Enhancements in the First and Second Hyperpolarizability of GMP Coordination Polymer: Crystal Structure and Computational Studies

Mubashar Ilyas [a], Maroof Ahmad Khan [b], Lin Xiong,[c] Li Zhang,[c] Muhammad Lauqman [a],Muhammad Abbas [d], Hafiz Muhammad Zohaib [a], Nagesh Manurkar [a], and Hui Li [a*]

[a] Key Laboratory of Clusters Science of Ministry of Education, School of Chemistry and Chemical Engineering, Beijing Institute of Technology, Beijing, 100081, P. R. China.

[b] State Key Laboratory of Marine Resource Utilization in South China Sea, Hainan University, Haikou 570228, China.

[c] Institute of Chemistry, Chinese Academy of Sciences, Beijing 100190, China.

[d] Advanced Research Institute of Multidisciplinary Science & School of Materials Science and Engineering, Beijing Institute of Technology, Beijing, China

Corresponding author name and Email:

Hui Li (lihui@bit.edu.cn)

1. **Experimental Section**
2. **Synthesis and Structural Characterization**
3. **Single-crystal X-ray diffraction data collection and structure determination**
4. **Circular Dichroism (CD) spectroscopy**
5. **Thermogravimetric Analysis (TGA)**
6. **Scanning Electron Microscopy (SEM) with Energy Dispersive X-ray Spectroscopy (EDS).**
7. **SHG Measurements**
8. **Hirshfeld Surface Analysis**
9. **Theoretical Study**
10. **NBO analysis**
11. **Quantum Chemical Descriptors**
12. **List of Tables**
13. **List of Figures**

1. Experimental Section

Material and Method

All chemicals used in the experiment were directly obtained from the market and did not require any purification process. Aladdin provided 1,2-bis(4-pyridyl) ethene, whereas Alfa Aesar supplied Co $(NO_3)_2$. $6H_2O$ and Guanosine-5′-monophosphate; disodium salt. FT-IR spectra were obtained using a Nicolet Nexus FT-IR spectrometer with KBr pellets covering the 4000–400 cm−1 range. Ultraviolet-visible (UV-Vis) spectra were recorded using a model TU-1950 spectrophotometer. We conducted powder X-ray diffraction (XRD) analyses using a Bruker D8 Advance X-ray diffractometer with graphite monochromatized Mo K radiation (λ = 0.71073). We used a Bruker APEX-II CCD and Rigaku Saturn724+ (2 × 2 bin mode) diffractometer for X-ray single-crystal data. We detected CD under a steady nitrogen flow using a JASCO J-810 spectropolarimeter.

2.Synthesis and Structural Characterization

An aqueous solution containing Co $(NO_3)_2 \cdot 6H_2O$ (0.04 mmol) was introduced to an aqueous solution of the Guanosine-5′-monophosphate disodium salt (GMP) to synthesize Complex (**1**) (0.04 mmol). The resulting mixture was stirred at room temperature for 30 minutes. Afterwards, a solution consisting of 1,2-bis(4-pyridyl) ethene (bpe) (0.04 mmol) in water was added to the reaction mixture. The resulting mix underwent further stirring and was subsequently filtered. HNO_3 was used to adjust the suspension's acidity to different pH levels (1M). We successfully grow the crystals of Complex (**1**) through the slow evaporation method at ambient temperature, which is suitable for X-ray diffraction (XRD) analysis after two weeks. The product yield, calculated based on the weight of GMP, was determined to be 78%. The complete process of synthesis of Complex (1) is represented in Scheme 1.

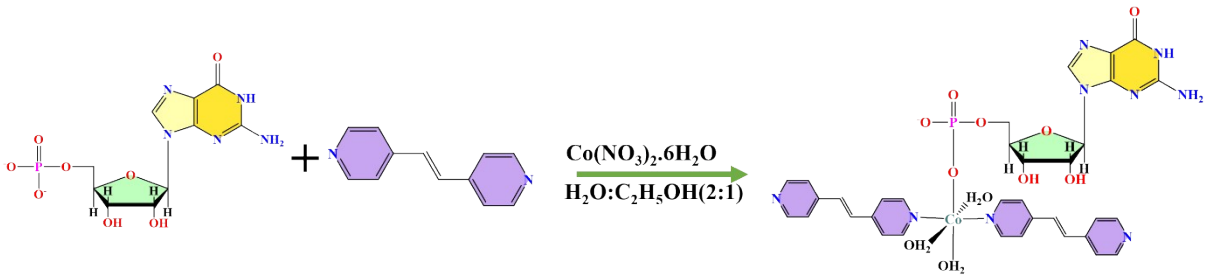

Scheme 1. The synthesis procedure of the complex (**1**).

3.Single-crystal X-ray diffraction data collection and structure determination

The X-ray single crystal diffraction data of the complex (1) was gathered using a Bruker SMART APEX2-CCD diffractometer. Graphite monochromatized molybdenum target Kα ray (λ = 0.71073 Å) served as the light source, maintaining a test temperature of 298 (2) K. Unit cell characteristics were determined and diffraction peaks were found using the XSCAN program, which was used for data collection at 50 kV and 30 mA. The ω-2θ scanning approach was employed to obtain the diffraction data, and an empirical absorption correction was applied to all of the collected data. At 296.15 K or 293.2 K, the crystals were maintained during the data-gathering process.

Using Olex2, the structures of the complex (1) were resolved with SHELXT. Structure refinement was subsequently carried out using SHELXL and a refinement strategy based on Least Squares minimization 32. Using the differential electron density function ($I > 2\sigma(I)$) and Fourier synthesis, all non-hydrogen atoms were found and modified. The differential electron density was used to determine the geometrical locations of hydrogen atoms bound to carbon or nitrogen. Water molecules' corresponding hydrogen atoms were arranged in geometrically reasonable locations. The least squares approach F2 was used to refine temperature factors (anisotropy/isotropy) and atomic coordinates.

4.Circular Dichroism (CD) Spectroscopy

Before conducting measurements on the circular dichroism (CD) spectra of complex (**1**), A combination of 1 mg of crystalline sample and 200 mg of finely ground KBr powder was compressed into a disk using a method described in the literature to perform solid-state CD measurements. The probe solution containing complex (**1**) (the concentration is 2.5×10^{-5} M) was prepared, and the resulting mixture of complex (**1**) solutions underwent ultrasound treatment for 5 minutes before CD measurements were taken.

5. Thermogravimetric Analysis (TGA)

Thermogravimetric analyses (TGA) were performed using a DTG-60H thermal analyzer for complex (**1**) and in a nitrogen atmosphere at 40 °C and 800 °C at a heating rate of 10 °min−1.

6. Scanning Electron Microscopy (SEM) with Energy Dispersive X-ray Spectroscopy (EDS).

The SEM images were acquired by scanning electron microscopy (SEM) (Zeiss Gemini SEM 360)

7. SHG Measurements

Measurements of single crystal nonlinear optics were conducted using a custom-built scanning microscope equipped with a femtosecond laser pump (Mai Tai HP, <100 fs, 80 MHz, 690–1040 nm) in reflection geometry, with both incidence and detection angles set at 45°. The linearly polarized and circularly polarized pumps were adjusted using λ/2 and λ/4 plates, respectively. The second-order nonlinear optical susceptibility of the single crystals was determined using benchmark KDP as the reference under identical measurement circumstances. Signals from the anterior surfaces were gathered. The polarization of the incoming light and the reflected second harmonic generation signal from both complex (**1**) and KDP is p-polarized. We assume that birefringence is insignificant and that the refractive index of air is 1. The electric field of the reflected second harmonic generation intensity from the front surface may be determined using the equation. The whole SHG measurement process was used as described by Jialiang Xu et al.[1]

8. Hirshfeld surface Analysis

Regarding crystal packing, the investigation of various non-covalent interactions is crucial as they offer valuable insights into the molecular arrangements within the crystalline material.[2] To explore these interactions, the Hirshfeld Surface analysis (HSA) is conducted using the software Crystal Explorer 3.1.[3] The HSA aims to delineate the spatial extent occupied by a molecule within a crystal, enabling the partitioning of the total electron density of the crystal into electronic densities corresponding to individual molecular parts. The HSA can be generated using various features such as shape index, curvedness, normalized distance (d_{norm}), di, de, and electrostatic potential, among others. Each surface provides valuable insights into non-covalent interactions. In a d_{norm}-based HSA, the surface is depicted in three colours: red, blue, and white. Red and white regions on the HSA indicate interatomic contacts where the distance between atoms is equal to or less than the sum of their van der Waals radii, respectively. Consequently, on the HAS, red, white, and blue areas signify strong, moderately weak, and minimal intermolecular interactions, respectively. The value range of the dnorm is from -0.796 to 1.865 Å. The dnorm illustrations of the complex (1) show many brick red spots, which provide information about the close contact (H-Bonds) within the complex (**1**). The close contact and hydrogen bonds with the neighboring molecules are shown in the form of dotted lines.

Apart from Hydrogen bonding, the other important interaction in chemistry is the π.. π interactions. We can visualize the π.. π interaction of our complex by plotting the HSA on a shape index. The value of shape index of our compound is -1.0 to 1.0 Å, as depicted in Figure S9b. To study π..π interaction by visualizing the shape index of the HAS, the triangular region of the shape index consisting of red and blue colour is imperative. The red and blue triangular regions in the shape index of HSA show the curved surface (arrangement of π atomic orbits upon a molecule) and u-shaped surface (indicating the presence of the ring within the crystal structure), respectively.

The other property of a crystal that we can explore by using the HSA is curvedness. Curvedness refers to the regions on the surface that exhibit a plat, disc-shaped morphology, closely resembling the molecular shape surface. Elevated curvedness values arise from the shape and edge-like curvatures, facilitating the identification of areas where interaction occurs between neighboring molecules. The blue framework delineates flat patches, indicating π..π stacking interaction within the crystal structure. The value of the curvedness surface in HSA lies in the range of -4 to 0.4 Å.

2-D fingerprint images provide imperative insights into the types of intermolecular contacts between atoms and help analyze the variations in these patterns, thereby highlighting crucial intermolecular connections within the entire crystal structure. The fingerprint plot specifically delineates close contacts among all molecular components and aids in discerning the distribution of the mapped surface areas. Figure S10 illustrates some potential fingerprint interactions on the Hirshfeld surfaces for the complex (1). The percentage of the conceivable interactions between neighboring atoms on the Hirshfeld surfaces, including H….H (37%), H…. O (23.2%), O…H (15.9 %), and N…H (4.1%).

9.Theoretical Study

All the theoretical studies were accomplished by Gaussian 09 software, [4] and analysis of these calculations was done using GaussView 06,[5] Multiwfn 3.8,[6] and Visual Molecular Dynamics (VMD) software.[7] The geometry of complex (**1**) was optimized by B3LYP functional and 6-311G* basis set. For complex **(1),** the pseudo functional method was used in which a 6-311G* basis set was used for the C, H, O, P, and N atoms, and the LANL2DZ basis set was used for Co metal. This method is imperative if any metal is present in the system. TD-DFT was employed to perform the electronic transition calculation with 20 selected states.[8] It is pertinent to mention here that it is an extensively used method that justifies the correlation between theoretical and experimental calculations. Apart from this, it provides a highly accurate insight of the complex (**1**) stability and reactivity. To determine the nature of the short- and long-range interactions, QTAIM and NCI studies were used.[9] Frontier Molecular Orbital (FMO), Natural Bond orbitals (NBO),[10] Density of states (DOS),[11] Molecular electrostatic potential (MESP),[12] and non-linear optical (NLO) properties were performed by using the abovementioned method.

To determine the complex (**1**) relative stability, the interaction energy was computed. The interaction energy of the complex (**1**) was extracted using the following equation.[13]

$$E_{int} = E_{complex\,(1)} - (E_{GMP} + E_{BPE}) \qquad (1)$$

Where $E_{complex\,(1)}$Is the total energy of the complex, E_{GMP} is the energy of the nucleotide, and E_{BPE} is the energy of the auxiliary ligand. The counterpoise (cp) correction approach was used to remove the basis set superposition error. The corrected basis set superposition (Eint cp) was determined using the following equation:

$$E_{int\,cp} = E_{int} - \mathrm{BSSE} \qquad (2)$$

The band gap (Eg), or the energy difference between the lowest unoccupied molecular orbital (LUMO) and highest occupied molecular orbital (HOMO), was used to determine the electronic stability of the systems. For example, it was computed using the following equation:

$$E_g = E_{LUMO} - E_{HOMO} \quad (3)$$

Apart from the energy gap, chemical parameters like the electrophilicity index (ω) are the main parameters that provide information about energy stabilization when a complex (**1**) gains extra charge from its surroundings. Other parameters related to FMOs like chemical potential (μ), chemical hardness (η), softness (σ), electronegativity (χ), maximum electron flow (ΔN), nucleofugality (ΔE_n), and electrofugality (ΔE_e) These were computed using the following equations.[13]

$$\mu = \frac{E_{HOMO} + E_{LUMO}}{2} \quad (4)$$

$$\eta = -(E_{LUMO} - E_{HOMO})/2 \quad (5)$$

The electronegativity of the complex (**1**) is computed using equation 6.

$$X = -(E_{LUMO} + E_{HOMO})/2 \quad (6)$$

$$IP = -E_{HOMO} \quad (7)$$

The vertical electron affinity is computed using equation 8.

$$EA = -E_{LUMO} \quad (8)$$

The chemical softness is computed using equation 9.

$$\sigma = \frac{1}{2\eta} \quad (9)$$

The dependence of first hyperpolarizability on oscillation strength, transition dipole moment and energy required for the transition from ground to excited state can be computed using equation 10.

$$\beta_{total} = \frac{f_0 \times \Delta\mu}{\Delta E^3} \quad (10)$$

Hyper-Rayleigh Scattering (HRS) was calculated using Equation 11.

$$\beta_{HRS}(-2\omega;\omega,\omega) = \left(<\beta_{zzz}^{2}> + <\beta_{zxx}^{2}>\right)^{1}/_{2} \quad (11)$$

The Depolarization Ratio (DR) of the complex (1) was calculated using equation 12.

$$DR = <\beta_{zzz}^{2}>/<\beta_{zxx}^{2}> \quad (12)$$

The degenerate four-wave mixing (γ^{DFWM}) computed using equation 13.

$$\gamma^{DFWM}(-\omega;\omega,-\omega,\omega) \approx {}^{1}/_{3}(ESHG)$$

$$+\gamma(dc-kerr) - {}^{1}/_{3}(\gamma(0;0,0,0) \quad (13)$$

The nonlinear refractive index of the complex (**1**) using B3LYP functional computed using equation 14.

$$n_2(\frac{cm^2}{W}) = 8.28 \times 10^{-23} \times \gamma^{DFWM} \quad (14)$$

10. NBO analysis

The NBO method is recognized as an effective tool for understanding atomic interactions, providing a robust framework for depicting charge transfer between occupied and unoccupied atomic orbitals.[14] Moreover, NBO analysis makes it easier to accurately depict charge densities and intramolecular delocalization between donor and acceptor groups. In NBO analysis, the stabilization energy of compound structures, based on second-order perturbation theory, can be calculated using the equation provided below.

In the equation above, the donor is denoted by (i), the acceptor by (j), and the stabilization energy by E(2). Additionally, the diagonal and off-diagonal orbital occupancies, along with the NBO Fock matrix elements, are denoted as follows: εi,εj, qi, and Fi,j, respectively. NBO analysis was conducted on Complex (**1**) and calculated using the B3LYP functionals, and their characteristics and interactions are summarized in **Table S5.**

Several prominent σ→ σ* transitions were investigated, including σ(C24-H25) → σ*(C6-N8), exhibiting higher stabilization energies of 2.79 kcal/mol in B3LYP functionals, respectively. Conversely, transitions such as σ (O9-H10) → σ*(C6-H7) were observed with minimal stabilization energies of 0.03 kcal/mol in B3LYP functionals, respectively. Other main transitions π→π* were investigated, including π(C40-C43) → π*(N14-C45), having higher

stabilization energies as 14.62 kcal/mol in B3LYP functionals, respectively. Conversely, transitions such as π(C40-C43) → π*(C29-C37) were observed with minimal stabilization energies of 5.66 kcal/mol in complex (**1**) computed using the B3LYP/GENECP method, respectively. Apart from this, some other transitions with high and low stabilization energies are shown in **Table S5.**

11. Quantum Chemical Descriptors

The global reactivity characteristics of a molecule, including its chemical hardness (η), chemical softness (σ), global electrophilicity (ω), electronegativity (X), ionization energy (I), and electron affinity (A), are greatly aided by the HOMO-LUMO energy gap. When evaluating the kinetic stability and reactivity of chemicals, these factors are essential. [15] Its capability for electron donation and acceptance may be estimated using a complicated ionization potential, which is the energy needed to remove an electron from the HOMO (Highest Occupied Molecular Orbital). This property is significant in demonstrating their ability to donate and accept electrons. One important chemical feature that governs a compound's propensity to draw in incoming electrons is its electronegativity. Chemical potential (μ) and chemical hardness (η) can be used to evaluate a compound's stability. From Table **S6**, it is evident that complex (**1**), exhibits a higher ionization energy (6.67 eV). Interestingly, complex (**1**) computed using B3LYP functional displays a greater electron affinity (A = 2.79 eV) with a smaller electronegativity (X =4.73 eV). Still, these metrics are comparable between complex (**1**) calculated using the GENECP basis set, indicating their significant ability to attract electrons. A compound's chemical hardness and energy gap are intimately correlated; in general, compounds with a higher energy gap are more kinetically stable, harder, less reactive, and resistant to changes in their electronic configuration. Compounds that have a smaller energy gap, on the other hand, are considered soft; they exhibit more chemical reactivity and poorer kinetic stability. Considering the information above, it is observed that complex (**1**) computed using B3LYP functional exhibits a larger value of global hardness (η = 1.93 eV) with a smaller value of softness (σ= 0.25 eV). These findings indicate that complex (**1**) computed using B3LYP functional is less stable and more reactive. The graphical representation of these descriptors is presented in Figure S11.

12. List of Tables

Table S1. The total number of hydrogen bonds extracted from the CIF file of the complex.

D–H–A	d(D–H)	d(H···A)	∠DHA	d(D···A)	A

O1–H1A–O5	0.92	1.84	146.4	2.662 (7)	
O1–H1B–O13	0.93	1.77	164.6	2.668 (8)	
O2–H2A–O15	0.86	2.04	150.5	2.820 (9)	-1+X,+Y,+Z
O3–H3A–O10	0.91	2.14	128.4	2.795 (7)	1+X,-1+Y,+Z
O9–H9–O5	0.82	1.90	155.8	2.669 (8)	-1+X,+Y,+Z
O10–H10A–O010	0.82	1.89	174.4	2.705 (11)	
O14–H–O6	0.85	1.92	150.2	2.690 (9)	
O15–HF–O13	0.85	1.92	155.1	2.714 (10)	
O13–HL–O4	0.85	1.90	153.5	2.687 (8)	1+X,+Y,+Z
O13–HM–O15	0.85	1.99	142.1	2.714 (10)	
O18–HO–O010	0.85	2.24	131.2	2.871 (17)	

Table S2. The comparison of the bond length of the complex extracted from CIF file and computed using B3LYP/GENECP level of theory.

Atom-Atom	**Bond Length (Å)**	
	Experimental	**B3LYP/GENECP**
O1-Co1	2.119(4)	1.901
P1-O4	1.524(4)	1.551
P1-O5	1.506(5)	1.584
P1-O6	1.510(5)	1.492
P1-O7	1.607(4)	1.664
Co1-N1	2.170(5)	2.009
Co1-O2	2.110(4)	2.074
Co1-O3	2.134(4)	2.251
Co1-O4	2.066(4)	1.956
C1-N1	1.357(8)	1.344
C1-C2	1.383(9)	1.385
N1-C5	1.329(7)	1.345
C2-C3	1.390(8)	1.406
N2-C10	1.345(8)	1.335
N2-C11	1.330(8)	1.339
N3-C18	1.294(8)	1.384
N3-C19	1.376(8)	1.385
C3-C4	1.394(8)	1.401
C3-C6	1.474(9)	1.462
N4-C17	1.477(7)	1.482
N4-C18	1.368(7)	1.384
N4-C20	1.361(7)	1.367
C4-C5	1.367(9)	1.382
N5-C20	1.346(8)	1.372
N5-C21	1.351(9)	1.393
C6-C7	1.314(8)	1.345
N6-C21	1.323(9)	1.374
O7-C13	1.444(6)	1.430
N7-C21	1.351(9)	1.295
N7-C22	1.379(9)	1.405
C7-C8	1.472(9)	1.464
O8-C14	1.452(7)	1.461
O8-C17	1.417(7)	1.411
C8-C9	1.390(9)	1.404

C8-C12	1.386(9)	1.402
O9-C15	1.398(7)	1.412
C9-C10	1.382(9)	1.388
O10-C16	1.419(7)	1.400
O11-C22	1.261(8)	1.374
C11-C12	1.393(9)	1.391
C13-C14	1.490(7)	1.525
C14-C15	1.535(8)	1.541
C15-C16	1.538(9)	1.527
C16-C17	1.538(10)	1.528
C19-C20	1.399(9)	1.370
C19-C22	1.408(9)	1.460

Table S3. The comparison of the bond angles of the complex extracted from CIF file and computed using B3LYP/GENECP level of theory.

Atom-Atom-Atom	Bond Angles (°)	
	Experimental	B3LYP/GENECP
O4-P1-O7	101.8(2)	101.2
O5-P1-O4	112.4(2)	108.5
O5-P1-O6	112.6(3)	113.1
O5-P1-O7	108.2(3)	104.5
O6-P1-O4	113.4(3)	118.2
O6-P1-O7	107.6(3)	109.5
O1-Co1-N1	88.49(17)	91.12
O1-Co1-O3	86.40(16)	97.3
O2-Co1-O1	173.78(17)	93.13
O2-Co1-N1	88.26(17)	99.35
O2-Co1-O3	88.36(16)	78.75
O3-Co1-N1	91.14(17)	93.47
O4-Co1-O1	88.74(15)	93.13
O4-Co1-N1	93.86(17)	166.50
O4-Co1-O2	96.77(16)	77.41
O4-Co1-O3	172.93(17)	98.65
N1-C1-C2	122.7(5)	122.58
C1-N1-Co1	122.8(4)	119.77
C5-N1-Co1	121.3(4)	122.25
C5-N1-C1	115.8(5)	117.75
C1-C2-C3	120.4(6)	120.31
C11-N2-C10	116.8(5)	116.63
C18-N3-C19	104.7(5)	105.44
C2-C3-C4	116.5(5)	116.30
C2-C3-C6	120.5(5)	124.38
C4-C3-C6	123.0(5)	119.31
C18-N4-C17	128.4(5)	131.56
C20-N4-C17	125.4(5)	122.53
C20-N4-C18	106.2(5)	104.62
C5-C4-C3	119.2(5)	120.20
P1-O4-Co1	137.9(2)	122.59
N1-C5-C4	125.4(5)	122.82
C20-N5-C21	112.4(5)	114.45
C7-C6-C3	125.8(5)	126.33
C13-O7-P1	120.2(3)	118.29
C21-N7-C22	126.4(6)	122.37
C6-C7-C8	126.8(6)	126.66
C17-O8-C14	110.7(4)	110.07
C9-C8-C7	124.1(6)	124.24
C12-C8-C7	119.6(6)	119.33

C12-C8-C9	116.3(6)	116.41
C10-C9-C8	120.0(5)	119.32
N2-C10-C9	123.5(5)	124.16
N2-C11-C12	122.9(5)	123.75
C8-C12-C11	120.5(6)	119.71
O7-C13-C14	108.5(4)	112.60
O8-C14-C13	109.7(4)	106.85
O8-C14-C15	104.5(4)	104.98
C13-C14-C15	115.9(5)	114.83
O9-C15-C14	111.6(4)	111.50
O9-C15-C16	115.2(5)	113.86
C14-C15-C16	102.2(5)	102.65
O10-C16-C15	108.5(4)	107.53
O10-C16-C17	110.9(6)	111.25
C15-C16-C17	102.1(5)	100.97
N4-C17-C16	113.4(5)	113.37
O8-C17-N4	109.1(5)	107.61
O8-C17-C16	107.3(5)	106.85
N3-C18-N4	113.8(5)	112.86
N3-C19-C20	110.0(5)	108.86
N3-C19-C22	131.5(6)	131.16
C20-C19-C22	118.4(6)	119.89
N4-C20-C19	105.3(5)	108.16
N5-C20-N4	126.9(5)	128.35
N5-C20-C19	127.7(6)	123.48
N5-C21-N7	122.7(6)	125.44
N6-C21-N5	119.2(7)	114.26
N6-C21-N7	118.1(6)	120.27
N7-C22-C19	112.2(6)	114.10
O11-C22-N7	119.2(6)	121.66
O11-C22-C19	128.6(7)	124.22

Table S4. The HOMO-LUMO gap, interaction energy and BSSE corrected energy of the complex computed using B3LYP/GENECP level of theory.

Complex (1)	HOMO (eV)	LUMO (eV)	E_g (eV)	Interaction Energy (Kcal/mol)	BSSE Correction (Kcal/mol)	BSSE Corrected Energy (Kcal/mol)
B3LYP	-6.67	-2.79	3.87	-286.69	24.01	-262.68

Table S5. The NBO analysis of the complex (**1**) using B3LYP/GENECP level of theory.

Method	donor(i)	type	acceptor(j)	type	E(2)[a][kcal/mol]	E(J)E(i)[b] (a.u)	F(I,j)[c] (a.u)
B3LYP	C24-H25	σ	C6-N8	σ*	2.79	1.02	0.067
	N27-C69	σ	C20-C68	σ*	2.79	1.27	0.079
	O9-H10	σ	C6-H7	σ*	0.03	1.23	0.007
	C59-H60	σ	P4-O23	σ*	0.03	0.812	0.007
	C40-C43	π	N14-C45	π*	14.62	0.27	0.079
	N14-C45	π	C50-C52	π*	13.52	0.32	0.083
	P4-O26	π	P4-O26	π*	0.63	0.59	0.025
	C40-C43	π	C29-C37	π*	5.66	0.29	0.055
	C12	LP (1)	C6-N8	σ*	67.5	0.1	0.122

	N36	LP (1)	N27-C69	σ*	9.2	0.72	0.104
	O35	LP (1)	P4-O26	σ*	0.03	0.86	0.007
	O49	LP (1)	C12-C16	σ*	0.04	1.21	0.009

Table S6. Quantum chemical descriptors of complex computed using B3LYP functionals.

Complex (1)	I	EA	M	η	σ	ω	X
B3LYP	6.67	2.79	-4.73	1.93	0.25	5.77	4.73

Table S7. QTAIM analysis of complex computed using B3LYP functionals.

B3LYP/GENECP level of Theory							
BCP	**Atoms**	**H(r)**	**ρ**	**$\Delta^2\rho$**	**V(r)**	**G(r)**	**-V(r)/G(r)**
74	O17…Co5	0.0058	0.038	0.25	-0.052	0.058	0.89
75	O1…H25	0.0022	0.023	0.091	-0.018	0.020	0.9
91	O23…H11	0.0021	0.032	0.14	-0.031	0.033	0.93
103	O34…H42	0.00090	0.033	0.12	-0.0305	0.0306	0.99
125	H7…O49	0.0016	0.011	0.044	-0.0077	0.0094	0.81
160	O39…H28	0.0015	0.011	0.043	-0.0077	0.0093	0.82

Table S8. Controlling factors of hyperpolarizability such as the ground state and crucial excited state (ΔE), change in dipole moment (Δμ), and oscillator strength (f_o), βtotal, α_{iso}, and α_{aniso}.

Molecules	f_o	λ_{max}	ΔE (eV)	α_{iso} (a.u.)	α_{aniso} (a.u.)	β_{total} (a.u.)	Δμ (a.u.)
B3LYP	0.0623	383.59	3.2322	396.62	305.48	2319.98	0.8554
P-NA	0.3640	330.21	3.7547	101.59	97.06	2048.34	0.0631

Table S9. The βHRS and DR values of the complex using B3LYP functional and P-NA molecule.

Frequency (a.u.)	**βHRS**	
	B3LYP	**P-NA**
0.04282	3801.046	1664.42
0.02389	1037.674	1070.238
Frequency (a.u.)	**DR**	
	B3LYP	**P-NA**
0.04282	5.089	4.476
0.02389	1.172	4.223

13.List of Figures

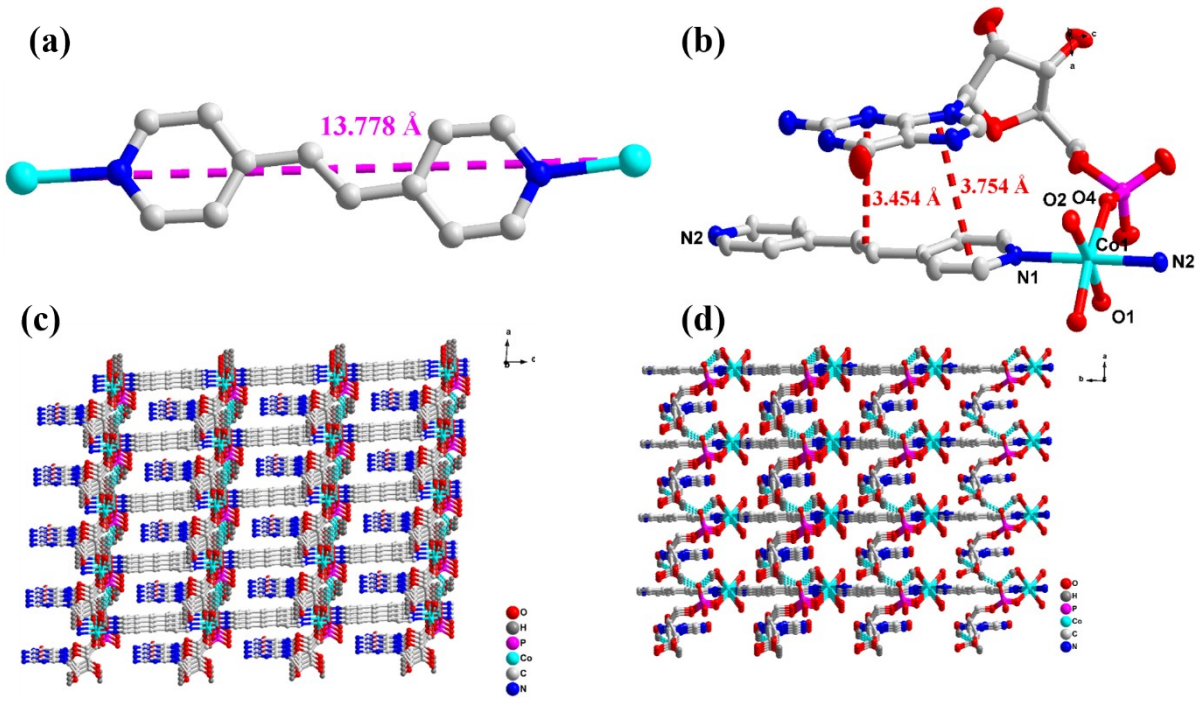

Figure S1. (a). The distance between two cobalt atoms separated by BPE ligand (b). Asymmetric unit showing the pi-pi stacking interaction (c,d). 3D chain of complex along b and c axis, respectively.

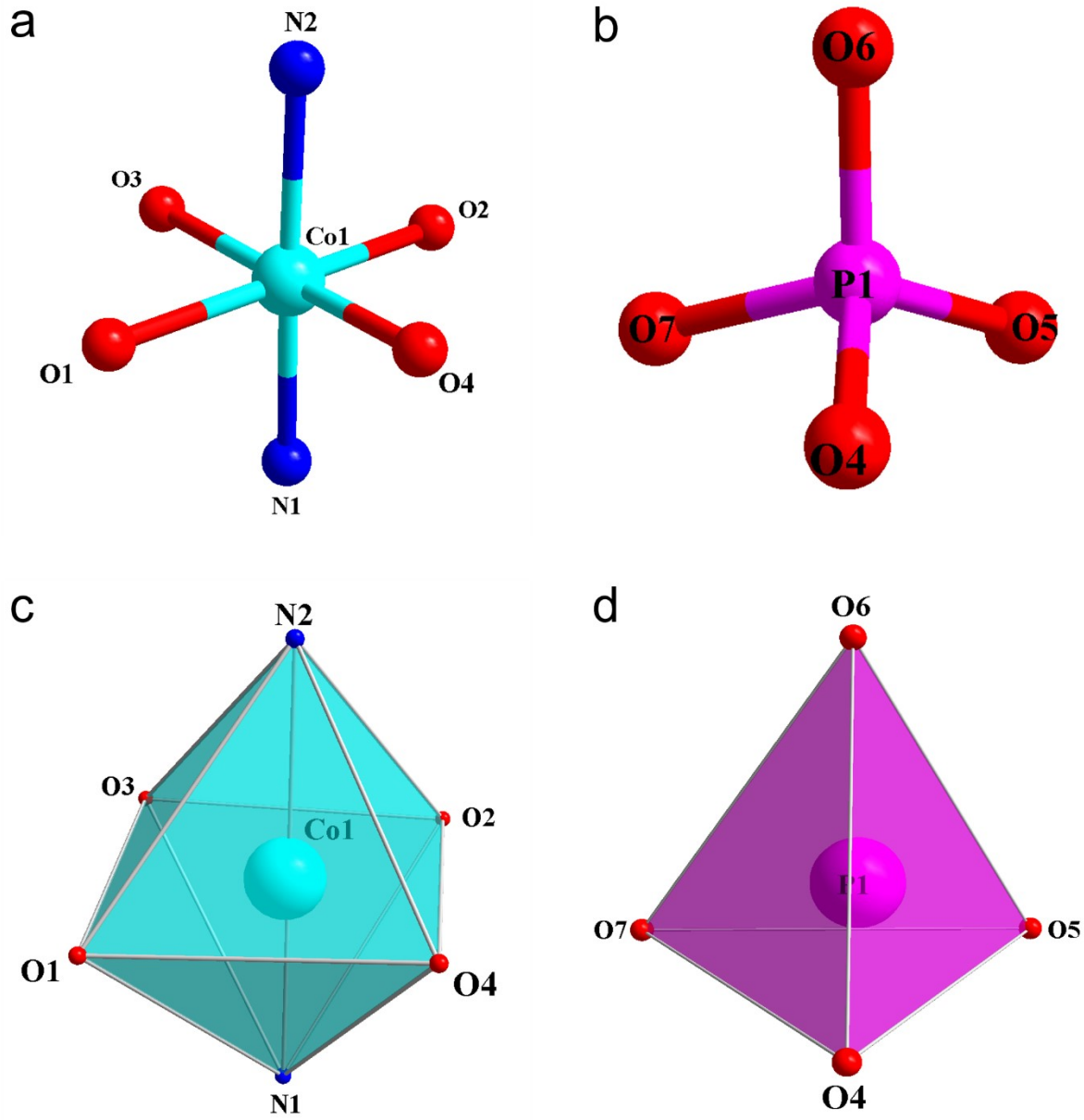

Figure S2. Distorted octahedra geometry (a) around cobalt and distorted tetrahedral geometry (b) around phosphorus and their polyhedral forms (c and d), respectively.

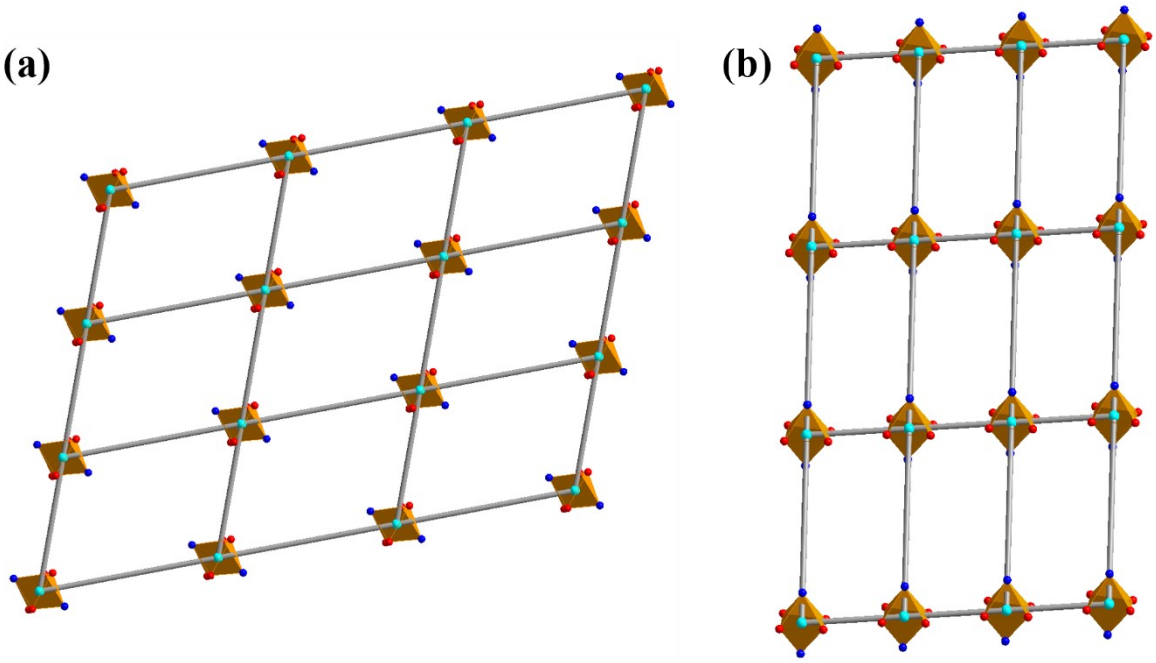

Figure S3. The 3D topological structure of complex (1) viewing along a and b-axis, respectively.

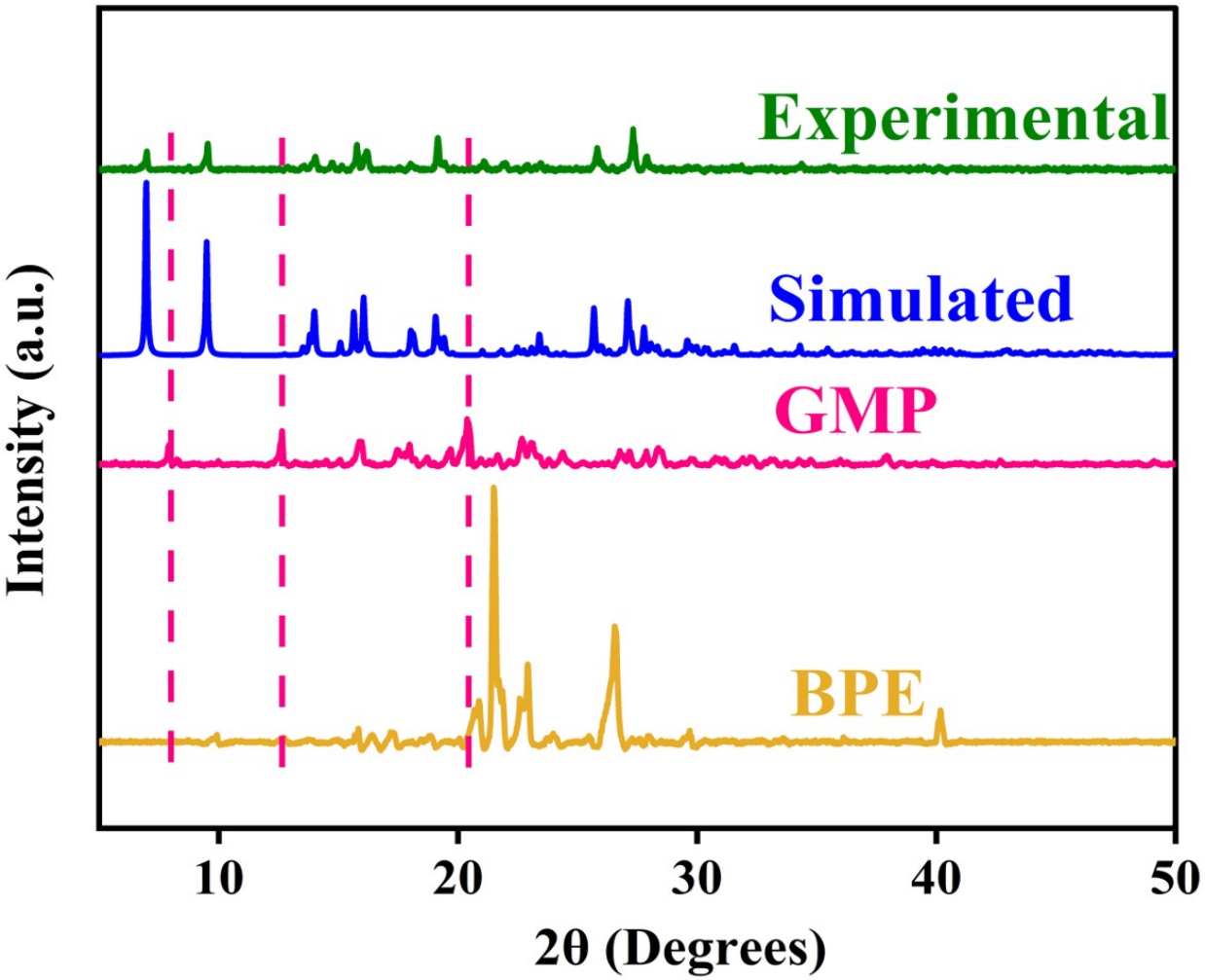

Figure S4. The PXRD data of the complex (**1**) and GMP and bpe ligands.

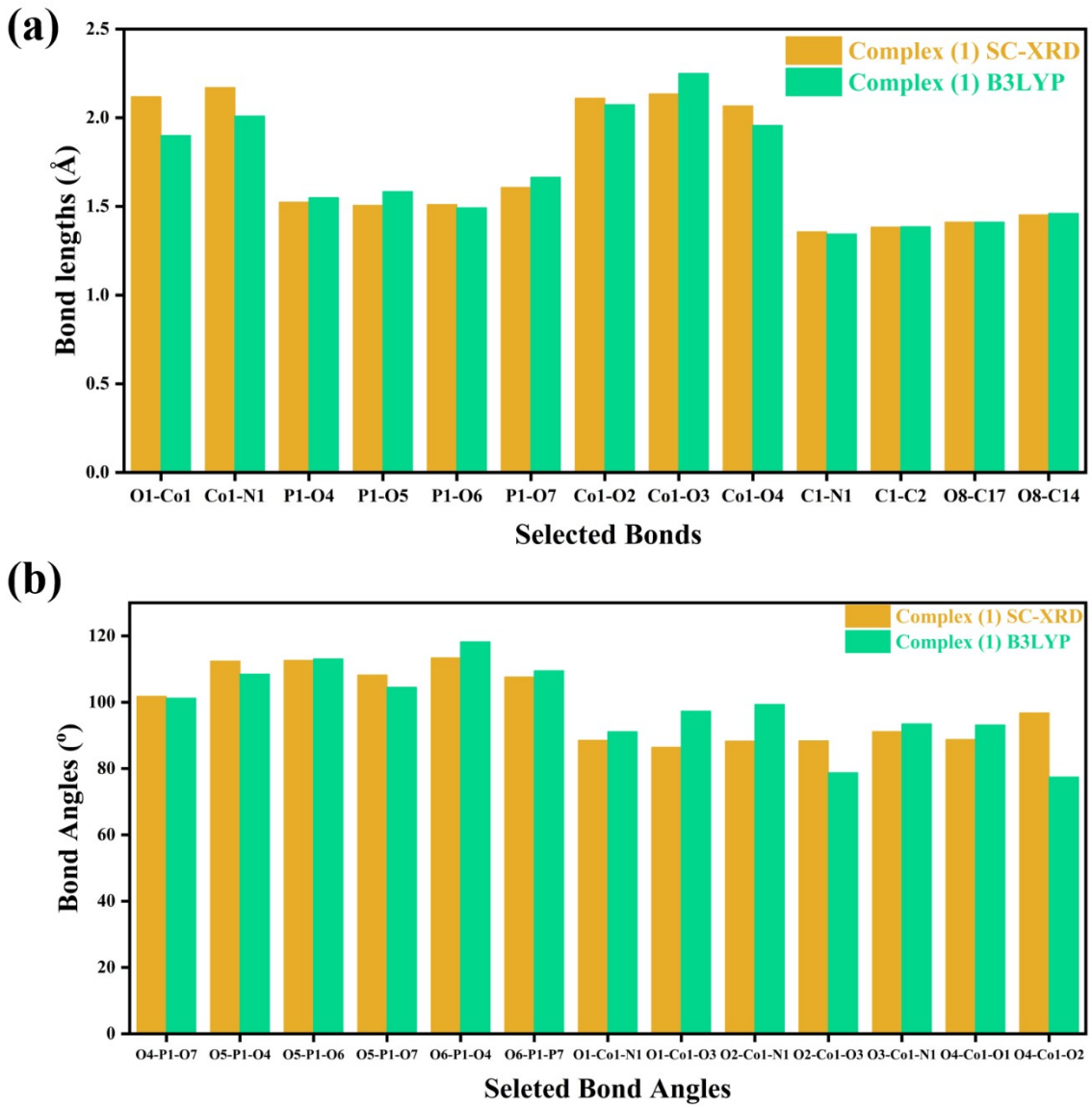

Figure S5. Comparison of the selected bond lengths **(a)** and angles **(b)** extracted from single crystal XRD data and data calculated using B3LYP/GENECP levels of theory.

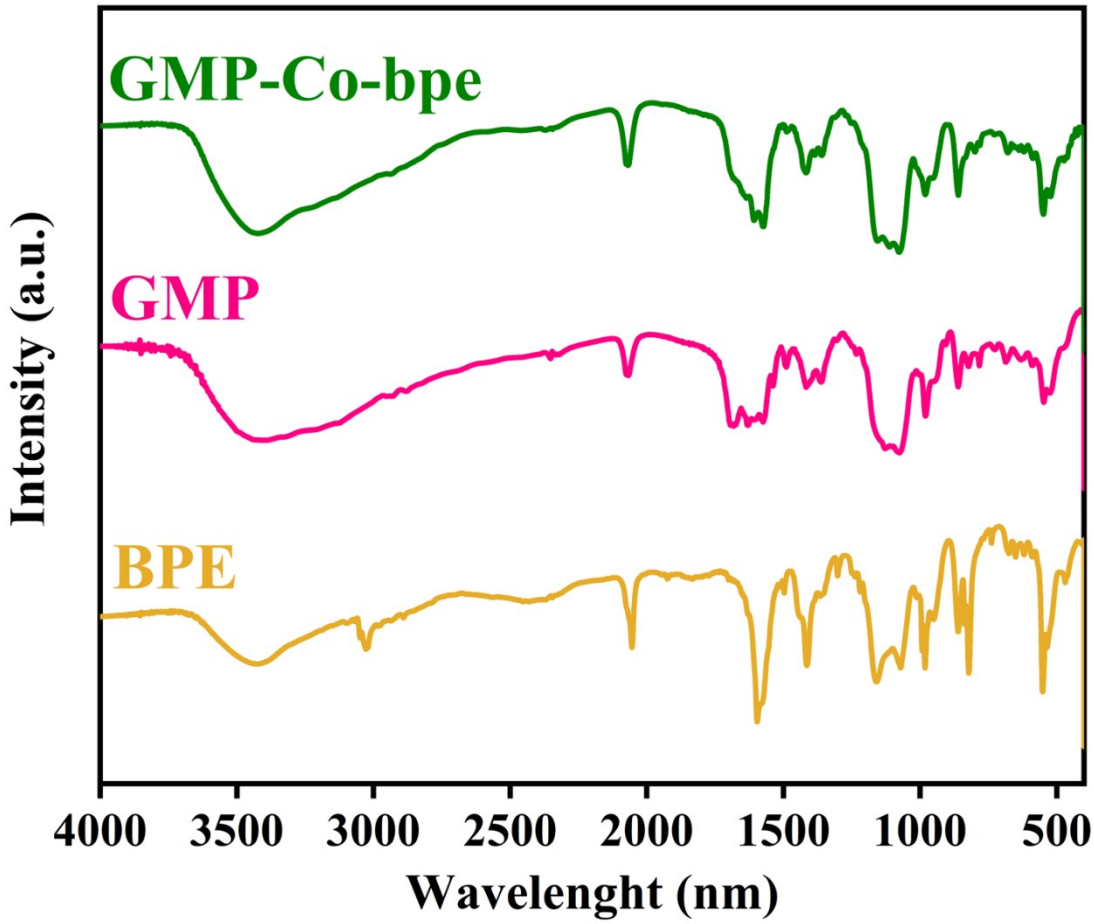

Figure S6. The FTIR spectra of complex, BPE and GMP.

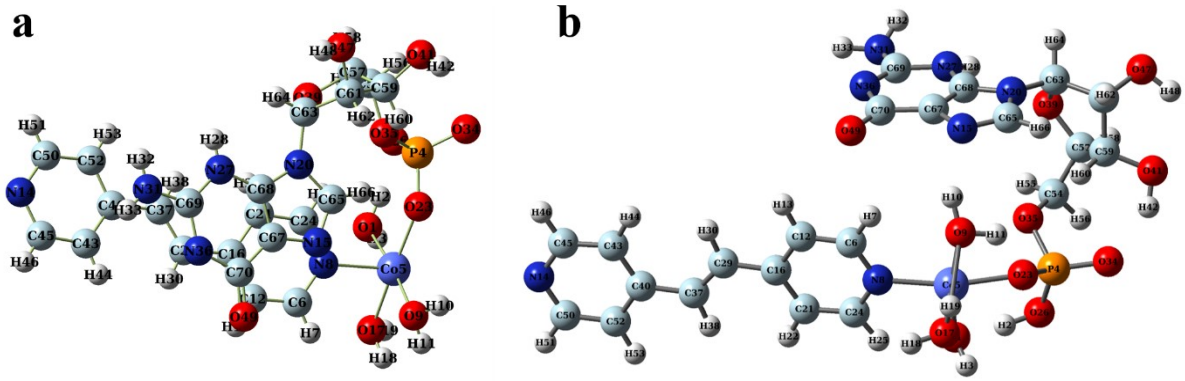

Figure S7. Structures of the complex extracted from CIF file (**a**) and computed using B3LYP/GENECP **(b)** level of theory.

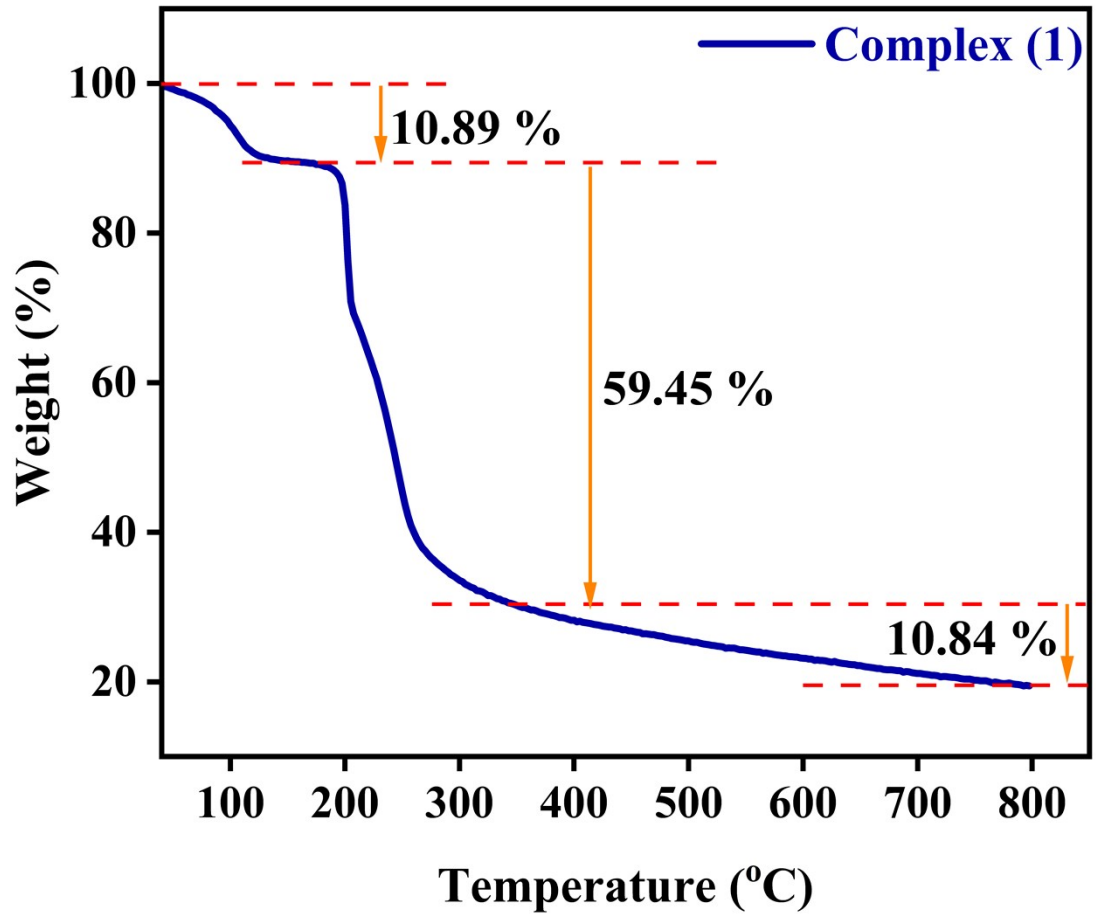

Figure S8. The TGA curve of the complex (**1**) shows the stability of the complex up to 800 °C.

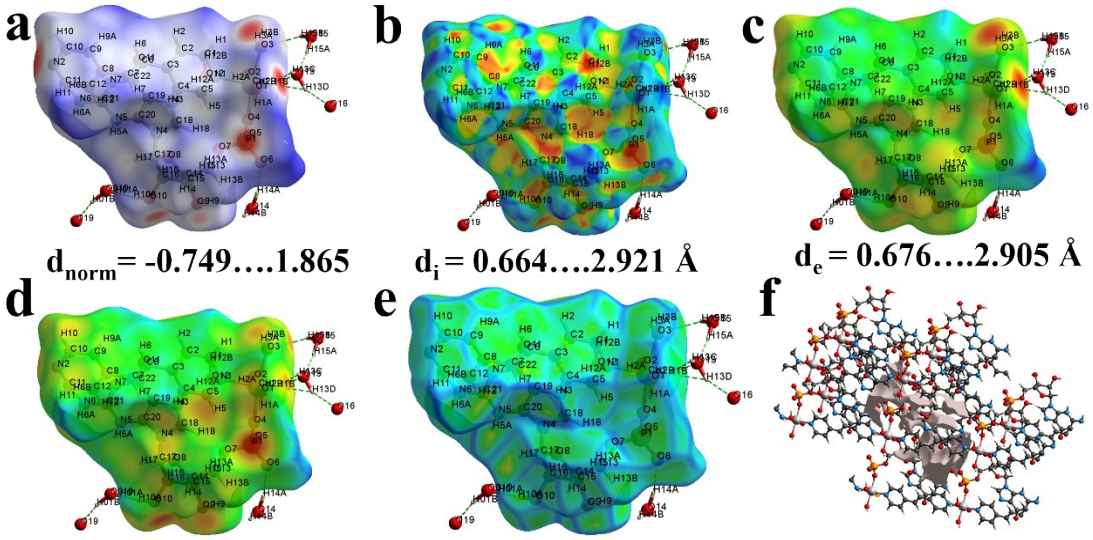

Figure S9.HSA plotted over different properties **(a).** d_{norm} =-0.749 to 1.865 **(b).** d_i =0.664 to 2.921 Å **(c).** d_e =0.676 to 2.905 Å **(d).** shape Index =-1.0 to 1.0 **(e).** Curvedness = -4.0 to 0.4 and **(f).** Void Volume =140.71 A^3.

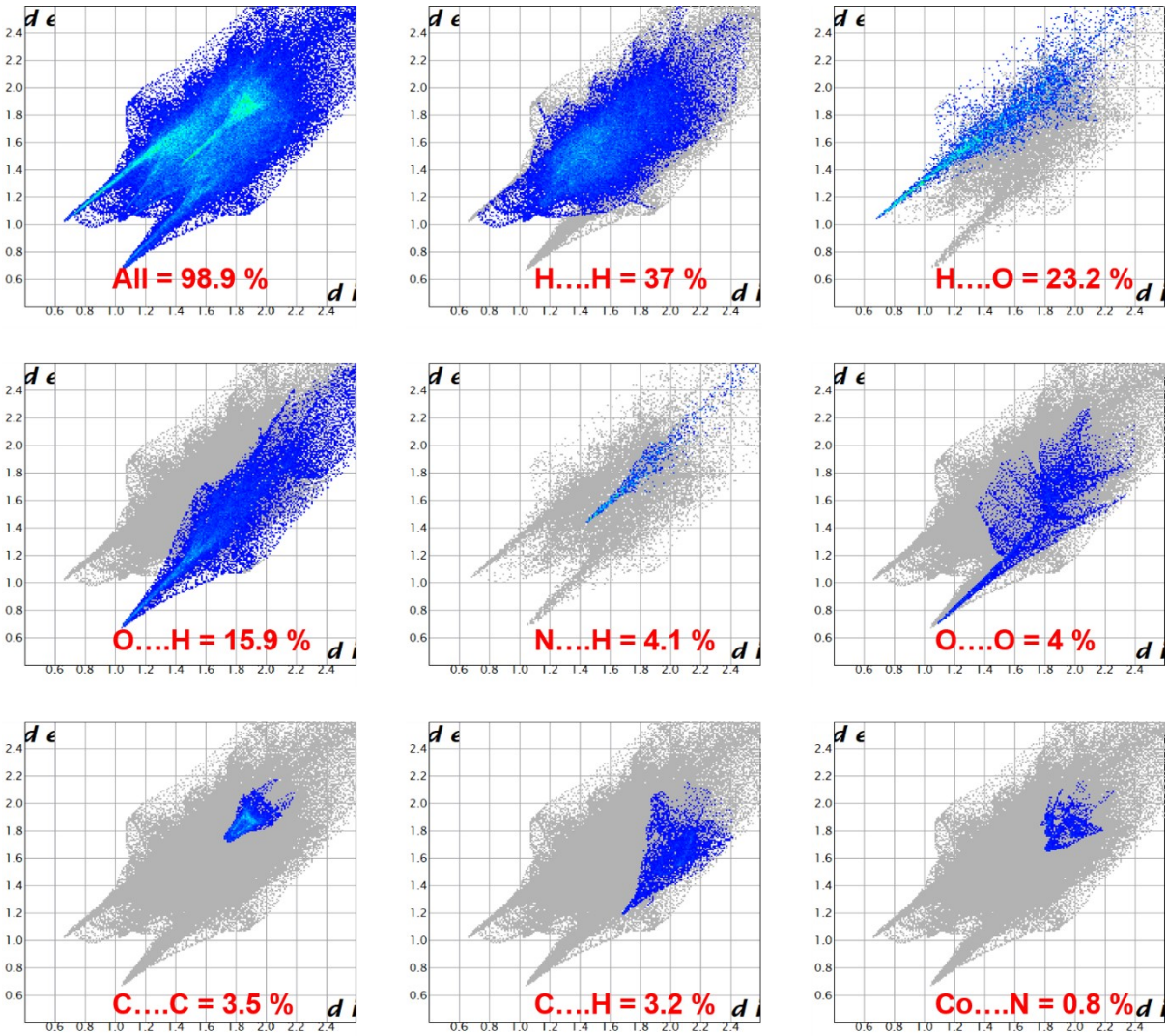

Figure S10. Crucial 2D finger plots of the complex (**1**) showing individual interatomic contacts and overall interactions.

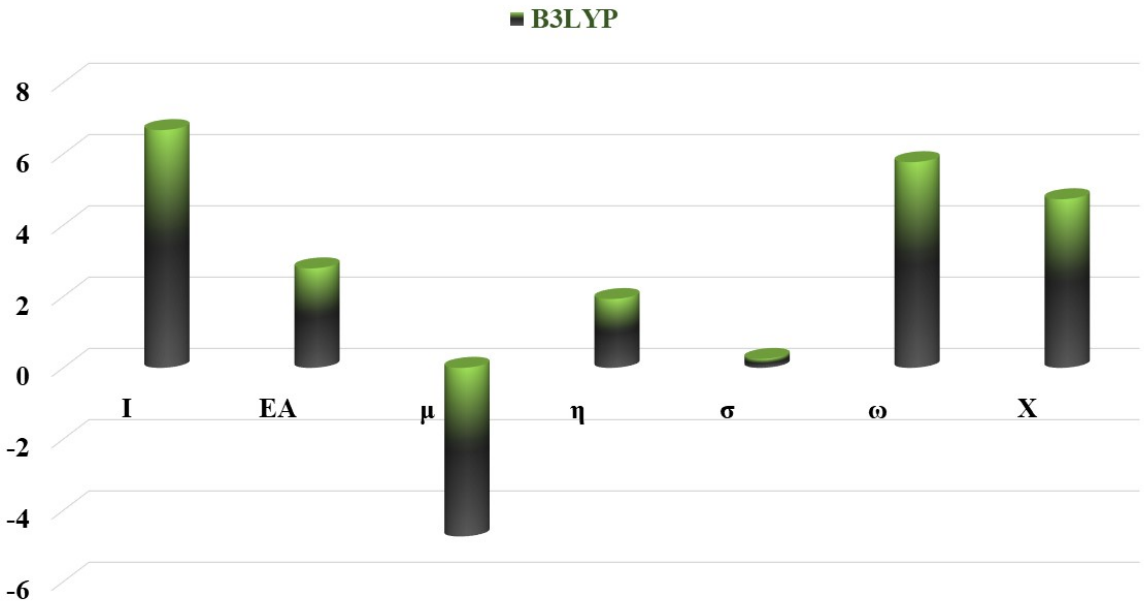

Figure S11. The graphical representation of the chemical descriptors of complex computed using B3LYP/GENECP level of theory.

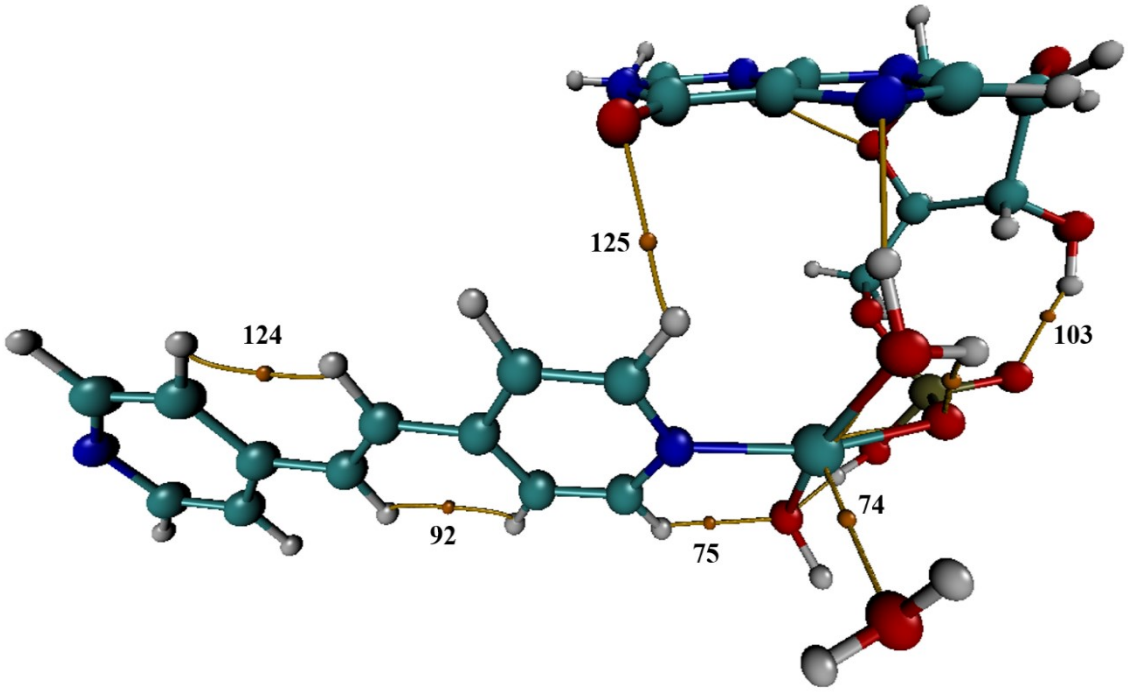

Figure S12. The QTAIM analysis of complex (**1**) computed using B3LYP/GENECP level of theory. The numbers 74,75,92,103,124 and 125 are the bond critical points (BCP).

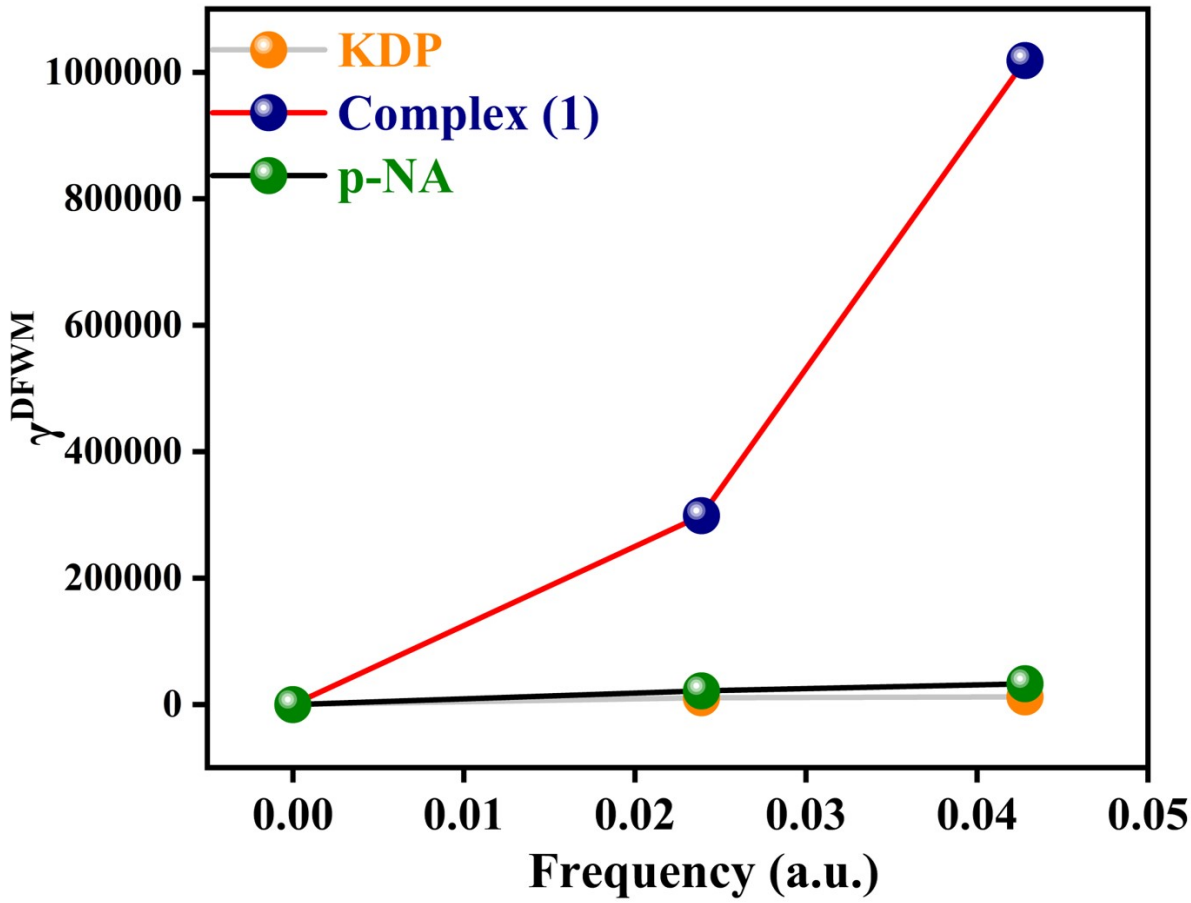

Figure S13. The comparison of the degenerate four-wave mixing (γ^{DFWM}) of complex computed using the B3LYP functional and P-NA molecule.

References

[1] P. Cheng, X. Jia, S. Chai, G. Li, M. Xin, J. Guan, X. Han, W. Han, S. Zeng, Y. Zheng, *Angewandte Chemie* **2024**, *136*, e202400644.

[2] M. A. Spackman, D. Jayatilaka, *CrystEngComm* **2009**, *11*, 19-32.

[3] P. R. Spackman, M. J. Turner, J. J. McKinnon, S. K. Wolff, D. J. Grimwood, D. Jayatilaka, M. A. Spackman, *Journal of Applied Crystallography* **2021**, *54*, 1006-1011.

[4] A. Frisch, *Wallingford, USA, 25p* **2009**, *470*.

[5] R. Dennington, T. A. Keith, J. M. Millam, *Semichem Inc Shawnee Mission KS* **2016**.

[6] T. Lu, F. Chen, *Journal of computational chemistry* **2012**, *33*, 580-592.

[7] W. Humphrey, A. Dalke, K. Schulten, *Journal of molecular graphics* **1996**, *14*, 33-38.

[8] A. D. Laurent, D. Jacquemin, *International Journal of Quantum Chemistry* **2013**, *113*, 2019-2039.

[9] F. Cortés-Guzmán, R. F. Bader, *Coordination Chemistry Reviews* **2005**, *249*, 633-662.

[10] E. D. Glendening, C. R. Landis, F. Weinhold, *Journal of computational chemistry* **2013**, *34*, 1429-1437.

[11] A. Heathcote, *Behavior Research Methods, Instruments, & Computers* **1996**, *28*, 427-445.

[12] R. A. Costa, P. O. Pitt, M. L. B. Pinheiro, K. M. Oliveira, K. S. Salomé, A. Barison, E. V. Costa, *Spectrochimica Acta Part A: Molecular and Biomolecular Spectroscopy* **2017**, *174*, 94-104.

[13] M. A. Khan, J. Iqbal, M. Ilyas, A. R. Ayub, Y. Zhu, H. Li, *RSC advances* **2022**, *12*, 6336-6346.

[14] F. Weinhold, C. Landis, E. Glendening, *International reviews in physical chemistry* **2016**, *35*, 399-440.

[15] P. Thanikaivelan, V. Subramanian, J. R. Rao, B. U. Nair, *Chemical Physics Letters* **2000**, *323*, 59-70.